Dimorphs of a Benzothiophene-quinoline Derivative with Distinct Mechanical, Optical, Photophysical and Conducting Properties

K. S. Bejoymohandas,[a,b,c] Ashish, A[e] Chithra H. Sharma,[f] Sunil SeethaLekshmi,[a] Kiran S. R. N. Mangalampalli,[g] Indira S. Divya,[a,b] Madhu Thalakulam*,[f] Filippo Monti*,[c] Rajesh V. Nair*,[e] Sunil Varughese*[a,b]

[a]Chemical Science and Technology Division, CSIR-National Institute for Interdisciplinary Science and Technology, Trivandrum, Kerala 695019, INDIA

[b]Academy of Scientific and Innovative Research (AcSIR), Ghaziabad 201002, INDIA

[c]Institute for Organic Synthesis and Photoreactivity (ISOF), National Research Council of Italy (CNR), Via P. Gobetti 101, I-40129 Bologna, ITALY

[d]Department of Chemical Engineering, Pohang University of Science and Technology, 77 Cheongam-Ro, Nam-Gu, Pohang, Gyeongbuk 37673, Republic of Korea

[e]Department of Physics, Indian Institute of Technology Ropar, Rupnagar, Punjab-140001, INDIA

[e]School of Physics, Indian Institute of Science Education and Research Thiruvananthapuram, Kerala-695551, INDIA

[f]Department of Physics and Nanotechnology, SRM Institute of Science and Technology, Chennai-603203, INDIA

Abstract

Because of distinct molecular conformations, packing modes, interaction types, and consequently their physicochemical properties, polymorphic forms of organic conjugated small molecules are intrinsically ideal for elucidating the relationship between their microstructures and the transcribed properties. Ethyl-2-(1-benzothiophene-2-yl)quinoline-4-carboxylate (BZQ) exists as dimorphs with distinct crystal habits—blocks (BZB) and needles (BZN). The crystal forms differ in their molecular arrangements—BZB has a slip-stacked column-like structure in contrast to a zig-zag crystal packing with limited π–overlap in BZN—and their photophysical and conducting properties. The BZB crystals characterized by extended π-stacking along [100] demonstrated semiconductor behavior, whereas the BZN, with its zig-zag crystal packing and limited stacking characteristics, was reckoned as an insulator. Monotropically related crystal forms also differ in their nanomechanical properties, with BZB crystals being considerably softer than BZN crystals. This discrepancy in mechanical behavior can be attributed to the distinct molecular arrangements adopted by each crystal form, resulting

in unique mechanisms to relieve the strain generated during nanoindentation experiments. Waveguiding experiments on the acicular crystals of BZN revealed the passive waveguiding properties of the crystals. Excitation of these crystals using a 532 nm laser confirmed the propagation of elastically scattered photons (green) and the subsequent generation of inelastically scattered (orange) photons by the crystals. Further, the dimorphs display dissimilar photoluminescence properties; they are both blue-emissive, but BZN displays twice the quantum yield of BZB. This study underscores the integral role of polymorphism in modulating the mechanical, photophysical, and conducting properties of functional molecular materials. Importantly, our findings reveal the existence of light-emitting crystal polymorphs with varying electric conductivity, a relatively scarce phenomenon in the literature.

Introduction

Because the physical, chemical, and mechanical characteristics of crystalline solids are intimately connected to their structures and interaction types, understanding the structure-property correlations is essential for designing and creating novel materials.[1-5] Though molecular design engineering *via* covalent modifications is a possible strategy to modulate the physicochemical properties of organic materials, this process is labor-intensive and time-consuming.[6-8] Hence alternative approaches to realize this goal is a welcome step.[9-11] The possibility of a chemical compound crystallizing in two or more crystalline phases with different molecular arrangements and/or conformations—*polymorphism*—could lead to various physical, chemical, and mechanical properties.[12-15] Identifying and utilizing crystal forms with optimal safety, solubility, and stability has significant industrial appeal and is vital for unique applications, especially in the pharmaceutical context.[16-18] Besides its commercial significance, polymorphism provides an unparalleled opportunity to derive structural correlations relating to a specific attribute, as this phenomenon involves only limited variable parameters.[19-21] The physicochemical and optoelectronic characteristics of crystalline molecular materials are significantly influenced by any variations in the crystal packing, intermolecular interactions, and degree of intermolecular overlap in a unique crystal form.[22] In molecular semiconductors, wherein van der Waals and weak electrostatic (*i.e.*, quadrupole) interactions are dominant factors, any changes in the molecular packing that alter the degree of π–π overlap could influence their photophysical and charge-transport properties.[23-25] The literature has only limited examples of these investigations, nevertheless.

The Gibbs Phase Rule only enables one thermodynamically stable polymorph of a material to exist at any given temperature and pressure.[26-30] Still, kinetic stability permits the

coexistence of several crystal forms at ambient temperatures. The serendipitous appearance of a thermodynamically more stable crystal form, following Ostwald's Rule of Stages, with unsolicited physicochemical properties in the later stage of product development, can be unnerving and troublesome.[31,32] The concurrent disappearance of the less-stable form is also not new; such instances have been central to several product withdrawals and patent litigations.[33,34] Not surprising that the realm of polymorphism can be frustrating and expensive, as highlighted by Bučar *et al.*, and represents one of the most active areas of modern solid-state chemistry.[32]

In our ongoing studies on the polymorphism in aromatics and polyaromatics, we studied this phenomenon in ethyl 2-(1-benzothiophene-2-yl)quinoline-4-carboxylate (BZQ) (detailed information on synthesis and structural characterization provided in ESI). Depending on the crystallization condition, BZQ exists as dimorphs with distinct crystal morphologies—block-shaped (BZB) and acicular (BZN). Block-shaped crystals of BZB have {001} as the major face, and it crystallized from an 8:2 ethyl acetate-hexane eluent collected in a beaker while doing the column chromatography. Interestingly, recrystallization of the compound or BZB invariably yielded acicular crystals, BZN, irrespective of the solvent systems and their combinations employed. Of note, with the formation of the acicular crystals of the stable form (BZN) in the lab, the metastable form (BZB) failed to reappear; all the attempts to reproduce the crystals of BZB ended up in the formation of acicular BZN. The higher crystal density (1.38 g/cm^3) of BZN with respect to BZB (1.32 g/cm^3) further highlights its stability. The crystals of the elusive BZB were subsequently obtained in a laboratory in South Korea from a freshly synthesized sample by the fast evaporation of a saturated 8:2 ethyl acetate-hexane solution from a petri dish.

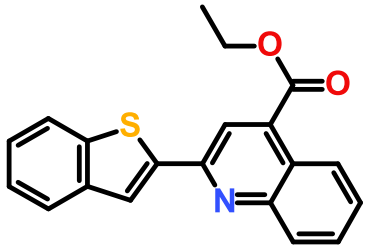

Scheme 1. The chemical structure of ethyl 2-(1-benzothiophen-2-yl)quinoline-4-carboxylate (BZQ)

Results and Discussion

Polymorphism: In the absence of classical interactions, weak and dispersive interactions such as C–H···O, C–H···π, π···π, S···π, and S···S interactions secure both the crystal forms. However, the crystal forms adopt different packing modes: the BZB has a slipped π-π stacking mode of the molecular organization against a zig-zag arrangement in BZN. Morphology predictions based on the growth vector or Bravais-Friedel-Donnay-Harker (BFDH) method propose [100] as the crystal growth direction in BZN (Figure 1) and (001) as the major crystal face with the lowest attachment energy (Table S1). In contrast, the comparable attachment energy for the standard crystal planes indicates the possible formation of block crystals in BZB.

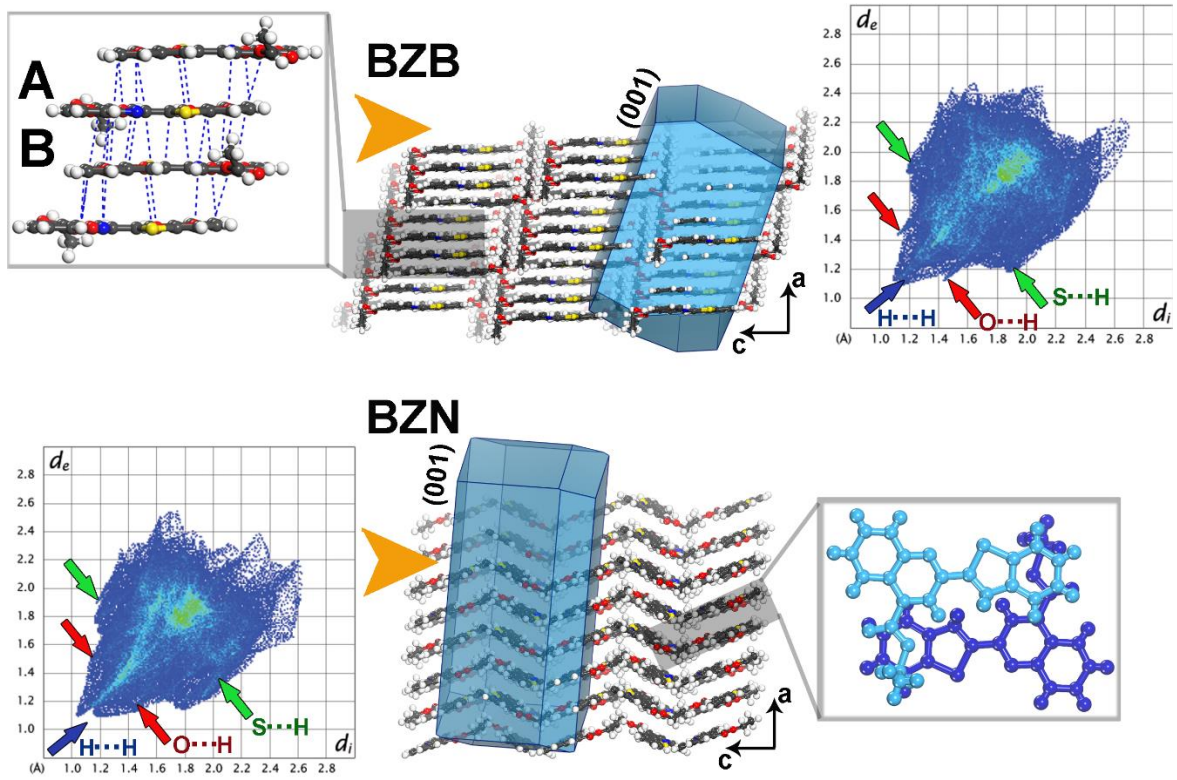

Figure 1. Crystal packing and molecular stacking with respect to the corresponding major crystal faces in the dimorphs BZB and BZN. While the molecules adopt an extended stacking in BZB, the zig-zag mode of packing in BZN has limited π-overlap. The fingerprint plot with major interactions are provided in inset. The indentation direction is represented as orange arrowhead.

Crystallized in a triclinic system ($P\bar{1}$) and with a single molecule in the asymmetric unit, (Table S2) the crystals of BZB have molecules arranged as a co-facial columnar structure in [100] direction. The average stacking distance is 3.58 Å. Placed in slip-stacks with a pitch angle of 21.02°, the molecular sheets along [101] present a minimal slip along the short axis (roll angle of 68.4°). Weak diffusional interactions stabilize the extended π-stacked molecular

columns. Two molecules in the asymmetric unit of BZN vary in the conformations of the ester ethyl moiety and the angles between the mean aromatic planes. The crystals of BZN have a zig-zag molecular arrangement against the stacked molecular columns in BZB. In BZN, molecules make dimers with an average intermolecular distance of 3.51 Å, but the adjacent dimers have minimal overlap. The structure, hence, is short of continuity along the molecular stacking direction [100].

Hirshfeld Surface (HS) Analysis: The HS and fingerprint analyses of the polymorphs show distinct surface and interaction characteristics;[35] the crystal forms have similar interactions, though their relative contributions vary. The energy framework analysis corroborates the dispersive characteristics of the interactions, with a negligible coulombic component.[36] The percentage contribution of H···O interactions ($C–H_{(ar)}\cdots O_{(C=O)}$ and $C–H_{(ar)}\cdots O_{(–O–)}$) in BZB and BZN are 7.7 and 4.1, respectively. The planar conformation of BZB (interplanar angle of 3.67°) and the extended molecular stacking lead to notable contributions from C–N and C–C interactions (14%). In contrast, with limited molecular stacking, BZN has lesser contributions from the stacking interactions (10.5%) (Figure S5). The H–H contribution in BZB is marginally higher vis-à-vis the stable BZN crystals.

The DSC thermograms of both forms exhibited a single endothermic melting event without evidence of any phase transformations (Figure S6 and S7). The onset of the melting curve of BZB is at 111.5 °C (ΔH_{fus} = 73.78 J/g), and that of BZN is at 114.8 °C (ΔH_{fus} = 86.12 J/g). The heat of fusion rule and a complementary slurry experiment validates a possible monotropic relation between the crystal forms.[37] The quantified nanomechanical response of crystal forms in terms of indentation modulus (*E*) and hardness (*H*) provide information on the elastic and plastic deformation mechanisms underneath the indenter tip.[38] The BZB crystals are softer than the crystals of BZN. The measured hardness, *H*, for BZB, is ~30% lower than that of BZN, indicating the tendency to undergo permanent deformation upon load application. The underlying crystal packing and molecular interactions (*vide infra*) are responsible for such observations.

BZB has columns of molecular stacks along [100], but the adjacent stacks separated by the ethyl ester moiety interrupt the formation of a continuous layered structure. Upon indenting the major face (001) of BZB, the tip traverses normal to the stacking direction; however, the discontinuity in the organization of the adjacent columns restricts its free movement. Molecules within the columns get compressed and slide along the slip direction [010]. Hence, the slip system realized for BZB is {001}<010>. Notably, though the load–displacement (*P–h*) curves for BZB and BZN penetrate to the similar depth under 6 mN load, their loading, unloading,

and creep (during the hold period) characteristics are disparate, demonstrating distinct mechanical behaviors. The pop-in events on the *P–h* curves obtained on the major face (001) of the BZB crystals manifest the discontinuity in the plastic deformation mechanism (Figure 2a). In contrast, upon indenting the major face (001) of BZN, the zig-zag molecular arrangement enables an accordion-type movement under the tip to dissipate the generated strain. This mechanism has limited molecular movement, unlike the long-range layer migration observed in BZB. Accordingly, the loading profile of the *P–h* curves corresponding to BZN are relatively smooth, and the pop-in events have lower dimensions vis-à-vis BZB. Further, the creep (time-dependent deformation under constant peak load) measures much higher for the BZB crystals than BZN, confirming their soft nature and tolerability to the indenter penetration without much resistance. Further, the weaker elastic recovery upon complete unloading for BZB crystals confirms the above analysis. Thus, based on the structural and mechanical response analyses, we posit distinct plastic deformation mechanisms adopted in the crystal forms (BZB and BZN) to release the strain incurred.

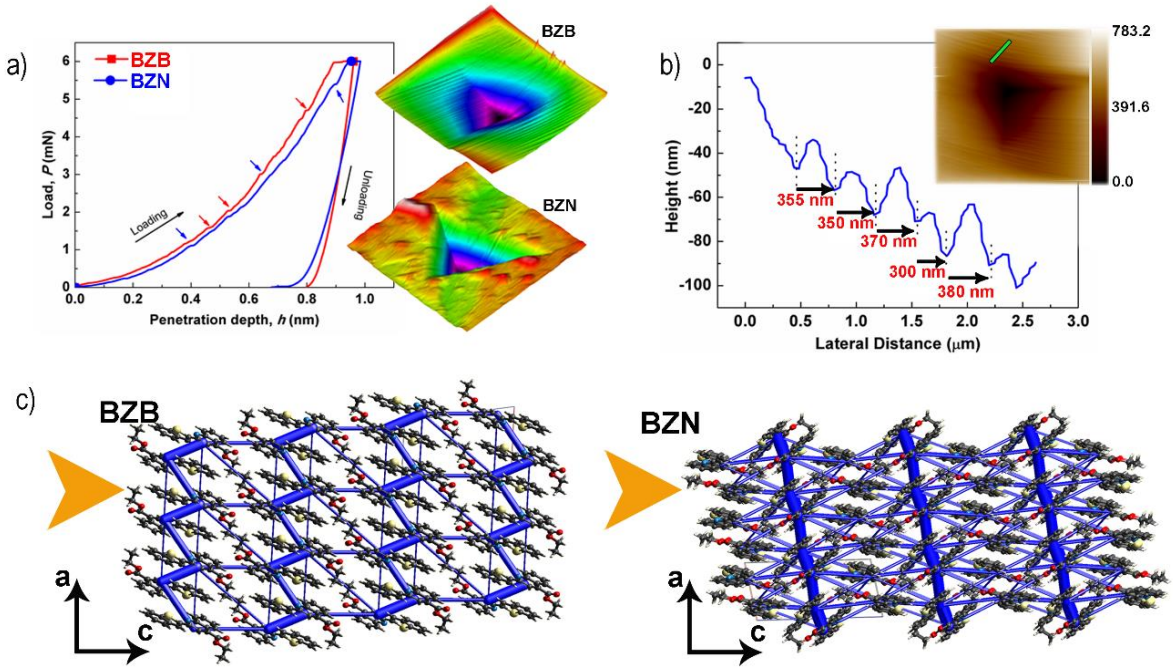

Figure 2. Nanomechanical properties of BZB and BZN. a) The load-displacement (*P–h*) curves obtained on the (001) faces of the dimorphs. The arrowhead on the loading curves corresponds to pop-in events. The post-indent scanning probe microscopy images obtained. Image scan size is 15.0 μm. b) Analysis of the distance between the two consecutive troughs on the periodic patterns formed on (001) face of BZB c) The total energy framework representation for the dimorphs. The thickness of each cylinder (in blue) represents the relative strength of interaction. The energy threshold for the energy framework was set at –20 kJ mol^{-1}.

The experimentally determined indentation modulus (E) of the crystals manifests the molecular packing, interaction types, and their relative orientations with respect to the indentation direction. Because similar interaction types describe both crystal forms but with different relative contributions, the E of the dimorphs differs only marginally (5%). The computed energy frameworks for the dimorphs highlight the dispersive nature of interactions (Figure 2c) and their well-segregated distribution that results in the commensurate magnitude of E. The observed marginal variations in the E could be related to the difference in the relative distribution and orientation of the interactions with respect to the indenter. BZN has a higher magnitude of H and E than the metastable BZB. The mechanical response also could be a determinant factor that could affect the overall stability of the crystal form. We noted a similar tendency in the crystal forms of aspirin, wherein the softer crystal form makes it more challenging to nucleate than the harder ones.[39]

Table 1. The mechanical and photophysical parameters of **BZQ**, **BZB,** and **BZN**.

Mechanical properties			**Photophysical properties**					
Sample	H (GPa)	E (GPa)	λ_{abs} (nm)	λ_{ems} (nm)	Φ_f	τ [b] (ns)	k_r [c] [ns^{-1}]	k_{nr} [d] [ns^{-1}]
BZQ[a]			300	446	0.15	1.00	0.15	0.85
BZB	0.185 ±0.05	10.23 ± 1.74	287	460	0.12	1.06	0.11	0.94
BZN	0.29 ± 0.01	10.77 ± 0.85	287	450	0.20	1.85	0.11	0.43

[a] BZQ was investigated in DCM solution; photoluminescence quantum yield was measured using the relative method with quinine sulfate (0.54) as standard. [b] Lifetime (τ), λ_{exc} = 375 nm. [c] Radiative rate constant: $k_r = \Phi_f / \tau$. [d] Non-radiative rate constant: $k_{nr} = 1 - \Phi_f / \tau$.

The post-indent scanning probe microscopy images on (001) of BZB show periodic patterns decorating the surface of the crystal on two of the three sides of the Berkovich indenter tip. The average measured distance between the adjacent peaks (~350 nm) correlates well with the average layer stacking distance in BZB (3.58 Å) (Figure 2b); it is indicative of a possible long-range molecular layer migration to the crystal surface along the edges of the tip. One could draw a resemblance between the layer migrations in BZB and that in the molecular complex of 1,2,4,5-tetracyanobenzene with pyrene.[40] However, a zig-zag model of the molecular arrangement in BZN forbids such a layer migration. The observed surface modifications further validate the proposed differences in the mechanisms of molecular rearrangements under the applied pressure. BZB and BZN have stronger interactions isolated from the weaker ones, which could immensely affect the mechanical response of the crystals.

Accordingly, the nanoindentation results highlight the softer nature of the crystal forms compared to the molecular crystals dominated by strong interactions or those having structures with strong and weak interactions interwoven to enhance the mechanical properties.[41]

Experimental and DFT photophysical investigation. The photophysical characteristics of the crystal polymorphs BZB and BZN as well as those of the single molecule BZQ in diluted dichloromethane solution, were investigated at room temperature. Moreover, to better rationalize the experimental findings, DFT calculations were also carried out both for the single molecule and crystals. The PBE0/def2-TZVP level of theory was adopted to investigate the single molecule, using the polarizable continuum model (PCM) to simulate dichloromethane solvation. Calculations show that the benzothiophene and the quinoline moieties of BZQ are fully coplanar, and only the carboxylate group deviates from planarity by 30.8°; notably, such deviation is also observed in the X-ray crystal structures, despite a lesser extent, most probably due to solid-state π-staking interactions. It is also worth noting that calculations confirm that the most stable conformer is the one having the nitrogen and sulfur atoms of the quinoline and benzothiophene rings in *cis*-arrangement (as found by X-ray diffraction), while the *trans*-conformer is 52 meV higher in energy, resulting in an 88:12 population ratio at 298 K. The Kohn–Sham molecular orbitals of the fully optimized BZQ molecule are reported in Figure 3a. HOMO and HOMO–1 are centered on the benzothiophene moiety; LUMO and LUMO+1 are predominantly localized on the quinoline part and show a remarkable double-bond character over both the C–C bonds connecting the benzothiophene and the carboxylate group with quinoline moiety. Consequently, charge-transfer transitions are expected to be dominant in BZQ, and planarization is likely to occur upon the relaxation of the lower-lying excited states.

Absorption and emission spectra of BZQ in room-temperature dichloromethane solution are presented in Figure 3b. The compound exhibits a vibronically unstructured absorption profile, showing two broad and intense bands with absorption maxima (λ_{max}) at 300 and 365 nm, assigned to the π–π* transition with strong charge-transfer nature, as suggested above. Indeed, TD-DFT calculations indicate that (i) such two bands can be mainly attributed to the $S_0 \rightarrow S_5$ and $S_0 \rightarrow S_1$ vertical excitations, respectively (Figure S8) and (ii) both transitions have a strong charge-transfer (CT) character from the benzothiophene to the quinoline moiety (Table S3). Upon excitation, BZQ displays a bright blue emission peaking at 446 nm, a photoluminescence quantum yield of 0.15, and a mono-exponential lifetime of 1.00 ns (Table 1). As shown in Figure 3b, the room-temperature emission profile of BZQ is broad and unstructured, as typical for CT transitions. Such a scenario is confirmed by the TD-DFT optimization on the S_1 excited

state, proving that BZQ undergoes a complete planarization even of the carboxylate moiety, which is expected to fade any potential vibronic progression of the associated fluorescence spectrum.

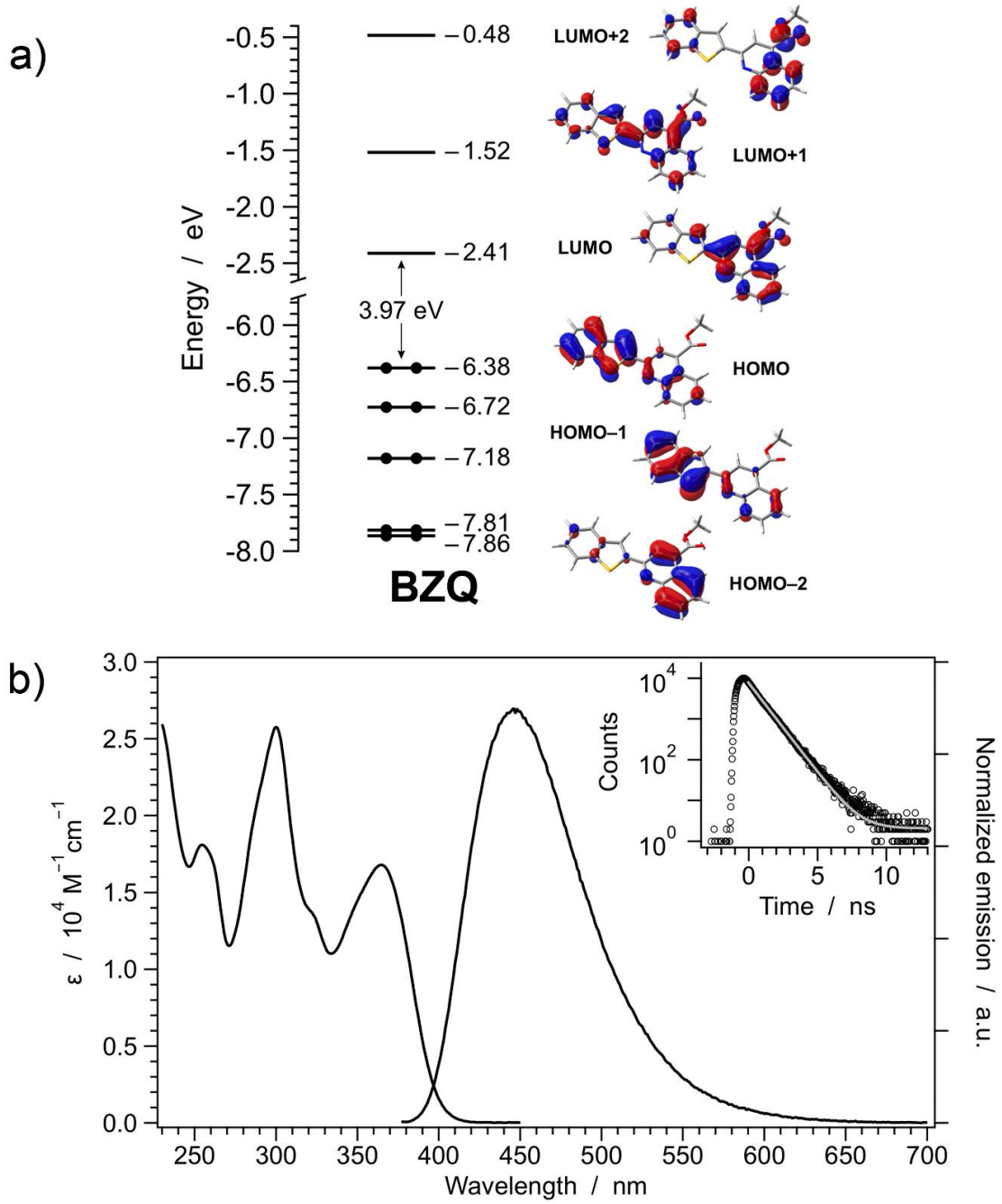

Figure 3. a) Energy diagram and selected Kohn–Sham molecular orbitals of the fully optimized BZQ in DCM. b) Absorption and photoluminescence spectra of BZQ in dichloromethane solution at 298 K (sample concentration ≈ 10 μM). The inset shows the fluorescence decay profile observed at the emission maximum.

In the solid state, the two polymorphs BZB and BZN, exhibit blue emission (Figure 4a-b), with unstructured profiles and luminescence quantum yields of 0.12 and 0.20, respectively (Table 1). Such findings are comparable to the ones observed for the single-molecule BZQ in solution, suggesting a similar emitting state as corroborated by comparable radiative decay constants (*i.e.*, k_r, see Table 1). Nevertheless, some minor distinctions are worth noting: (a) BZB shows a 0.08-eV red-shifted emission maximum as compared to BZQ, and (b) BZN displays a higher quantum yield, with a correspondingly elongated excited-state lifetime (Table 1). The bathochromic shift observed in the emission spectrum of BZB compared with that of BZN is qualitatively consistent with the π–π stacked columnar structure of the former. We also carried out DFT calculations on the 3D crystal structures of both dimorphs at the PBE-sol level of theory, to get a more rigorous picture of their electronic properties (see Experimental Section for further details).

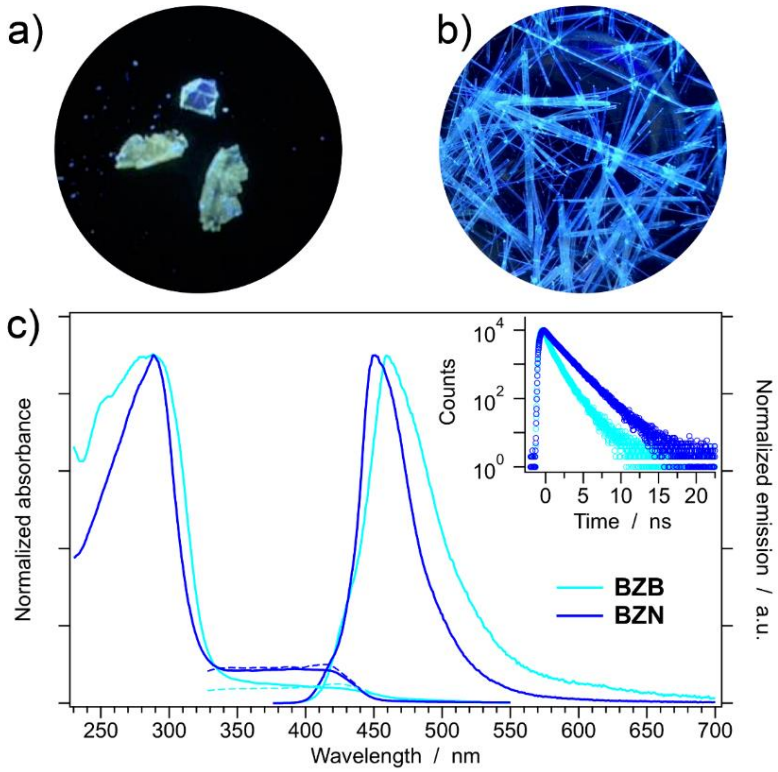

Figure 4. Crystals of BZB (a) and BZN (b) under the 365-nm UV light. (c) Solid-state absorption and emission spectra of BZB and BZN at 298 K; their emission decay profiles are also reported in the graph inset.

The DFT-optimized crystal structures of BZB and BZN as represented in Figure S9 and S15 show a good superposition with the X-ray diffraction data. Notably, such calculations show that both polymorphs display very similar band gaps (Figure S11 and S12), in agreement with

nearly superimposable emission spectra (Figure 4c). The DFT-computed band gap is underestimated (*i.e.*, 1.92 *vs.* 2.75 eV), as commonly found when using LDA or pure GGA functionals.[42] As in the case of single-molecule BZQ, the four upper valence bands of BZB are located on the benzothiophene moieties of the columnar stacks, as seen in the HOMO and HOMO–1 of BZQ; on the contrary, the four lower conducting bands are predominantly localized on the quinoline moiety, as for LUMO and LUMO+1 of BZQ (compare Figure S11 and 3a). This scenario is consistent with two molecules in the crystal cell of BZB. To be specific, along the Γ–X direction in the crystal momentum space (corresponding to the columnar packing direction), the highly interacting valence bands display the typical "folded pattern" profile of dimers with Peierls distortions (*i.e.*, band #118 is coupled with #116 and arise from the HOMO of BZQ, while HOMO–1 orbitals generate bands #117 and #115, see Figure S11).[43] On the other hand, the conduction bands do not strongly couple since orbital pairs are located on nearby molecules but of separated columnar stacks, which are insulated by the ethyl-esters chains (Figure S11).

The band diagram of BZN (Figure S12) is visually more complicated since four molecules are present in the unit cell. Still, the scenario is qualitatively similar to BZB (compare Figure S11 and S12). One should note that BZN displays a direct gap in the Y momentum space. At the same time, BZB is formally an indirect-gap semiconductor (despite the minimal energy difference along the Γ–Z path). Accordingly, as experimentally found, BZN displays nearly twice the photoluminescence quantum yield of BZB (Table 1), in which the emission of a photon must also be coupled with a phonon (despite a very low-energy one).

Optical waveguiding properties: Under excitation by a UV lamp, the long ends of the crystal exhibited much stronger emission than the body, indicating the optical confinement of emitted light within the crystal. The brightening at the tips of the acicular crystals of BZN indicates possible one-dimensional propagation of light through the crystals—optical waveguiding (OWG). Most of the reports on the waveguiding experiments are based on excitation with UV lasers inside the electronic absorption window which electronically excite the molecular constituent of the crystalline solids to fluoresce; the emitted light traverse to the crystal ends—*active waveguiding*.[44,45] Alternately, organic waveguides can work analogous to commercial optical fibers wherein the input light transmits directly to the output end along the organic medium—*passive waveguiding*.[46] In passive waveguiding, visible lasers with longer λ than the molecular absorption window avoid photoluminescence and provide information about the confinement and propagation of the guided laser photons. The visible energy photons

could trigger the weak Raman vibration modes due to inelastically scattered Stokes photons during the direct laser light propagation inside the molecular waveguide.[47,48] In contrast to first-order Rayleigh scattering, Raman scattering is a second-order process, and as such, the intensity of the scattering is weak. Because the Raman scattering cross-section is weak, it minimizes the optical loss inside the organic waveguide. Raman scattered photons can monitor the route of the guided input light within the organic crystals and find any nano or microscale fault spots.[49]

Because of the substantial index contrast ($\Delta n \sim 0.6$) of the acicular crystals, we expected efficient laser light coupling to the crystal, resulting in strong optical confinement by guiding the laser light along the crystal length. The acicular crystals showed maximum absorbance at 290 nm and emission at 450 nm (λ_{ex} = 414 nm). The shape of the solid-state absorbance band of BZN showed that there is no possible molecular absorbance above 450 nm. A home built optical setup using CCD camera and objective lens was used to study the OWG properties of the crystal (Figure 5a). The incident green photons from 532 nm laser were efficiently coupled with the crystal using a low magnification objective lens (20X; NA 0.4). Two in-situ camera positioned orthogonally were used to accurately focus light at the input of the crystal and to image the light propagation through the crystal (Figure S13). To reduce Rayleigh-scattered photons for analyzing the scattering phenomena resulting from laser light-organic crystal interactions, the camera images were simultaneously recorded using a color eyepiece video camera with a 532 nm long-pass edge filter. Orthogonal illumination of a green light laser beam at one of the end of the crystal and body of the needle showed propagation of guided photons to the opposite end of the crystal. Similar experiments performed on needles having an approximate length of 4.5 mm showed comparable results. The laser at the incident point on the crystal and the other end of the crystal both showed strong, inelastically scattered (low energy) orange photons, which is interesting (Figures 5b and 5c, respectively). The collected images with and without filters confirmed the propagation of elastically scattered photons (green) and subsequent generation of inelastically scattered (orange) photons by the crystals as green photons propagate along the crystal length (Figure 5d). The broad orange glow at the crystal end is due to the scattered photons coming out of the crystals while the intense center spot indicates the guided light through the crystal. The bright intensity at crystal ends and edges for both elastically and inelastically scattered photons is a signature of OWG property of the crystal. To quantify the OWG efficiency, the crystal was excited at various distances from the tip of crystal and the outcoupled photons from the tip were recorded using the fiber coupled spectrometer (Avantes, AvaSpec-3648). The decrease in the intensity of inelastically scattered

photons indicates the propagation losses, while the spectral shape remains unchanged (Figure 5e). An optical loss coefficient, α (mm^{-1}) of individual crystals was calculated by fitting the single exponential decay of the intensity with distance using the equation: $I_{body}/I_{tip} = A \cdot \exp(-\alpha d)$, where d represents the distance between the tip and the excitation spot on the body of crystal, which is the propagation distance before the emission was collected from the tip (Figure 5f). The optical loss coefficients determined for the individual crystal (0.99 dB/mm) indicate good waveguiding performance. The light propagated along the crystal length irrespective of the point of illumination, but the emission intensity varied inversely with the distance between the record tip and the excitation position (Figure S14). The BZN crystals do not show the lasing property as we did not observe any reduction in the full-width half-maximum (FWHM) at high pump power, though the signal intensity increased.

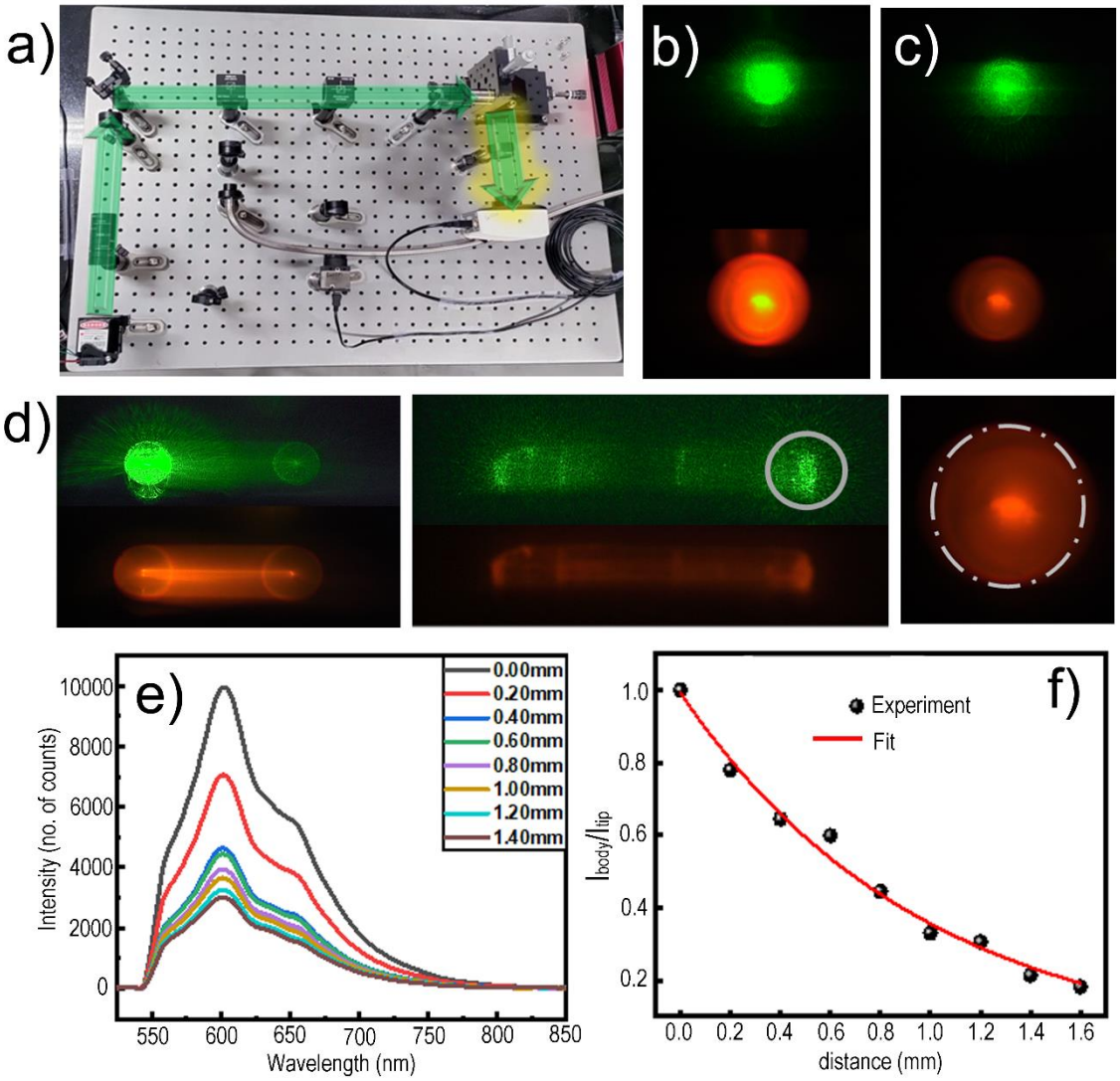

Figure 5. a) Waveguiding experimental setup. The green arrow highlights the directions of the laser beam. Point of illumination at b) edge of crystals and c) body of crystal and the corresponding fluorescence images (532 long pass). d) Crystal illuminated under 532 nm

and the fluorescence from the sample (532 long pass). e) Loss measurements and f) variation of the peak intensity at 532 nm *vs* the propagation distance for microrods of BZN.

Conductivity: The electrical conductivity (σ) of the dimorphs was measured; in a typical experiment, the crystals were contacted using silver paint, dried, and measured using a source measure unit in a two-probe configuration. The measurements were conducted at room temperature with the sample chip holder placed inside a Faraday cage. Figure 6 displays the measure I–V characteristics of the two crystal forms at room temperature. The linear relationship suggests that the I–V behaviour of **BZB** obeys Ohm's law at low applied voltage, and a nearly ohmic contact exists between the crystal and the electrodes. Crystal polymorphs that are light-emitting with varying electric conductivity are little reported, and most of them are insulators.[50,51]

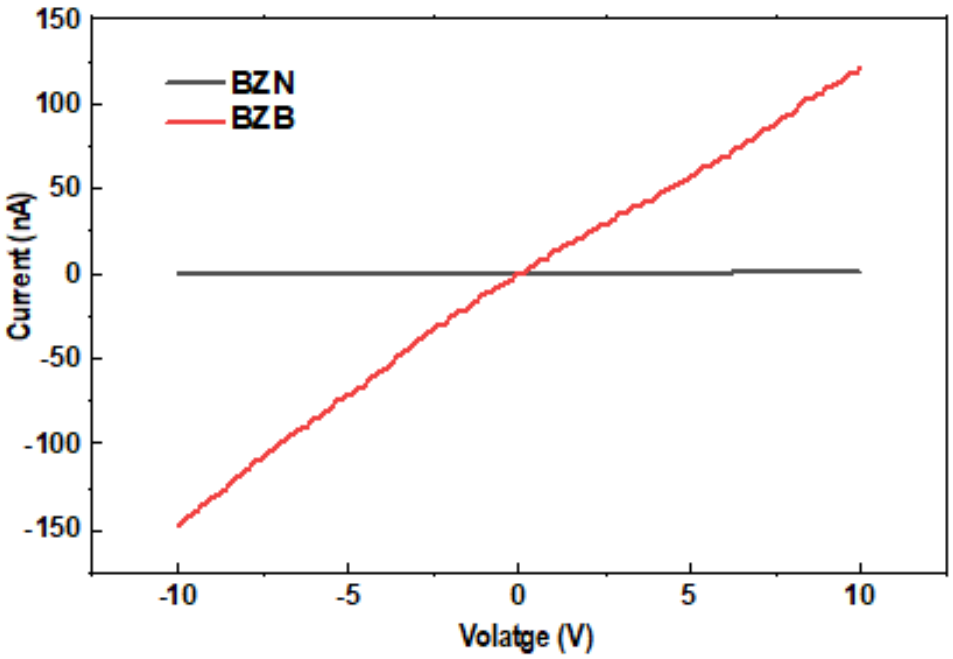

Figure 6. The I–V characteristics of BZB and BZN measured at room temperature

The **BZB** crystals with extended π-stacking along [100] (a measured resistance of ~80 MΩ) proved to be a semiconductor, while the **BZN** having a zig-zag packing mode with limited stacking characteristics (and with a resistance of ~30 GΩ) was reckoned as an insulator, under the investigated conditions.[52-54] This can be better understood by comparing the band diagrams of both polymorphs (Figure S11 and S12). Indeed, the highest valence band of **BZB** display very high velocities, which are maximized along the *k* paths having a strong X component (*i.e.*,

through the direction of the columnar packing); on the other hand, low-energy conduction bands do not present such high velocity values, suggesting that **BZB** has good hole mobility and less favorable electron mobility. It should be also emphasized that the group velocity in the Γ–Z direction is almost zero for the frontier bands of **BZB**, proving that the ethyl-carboxylate chains are able to fully interrupt the electronic communication between nearby columnar π-stacks (Figure S15).

Conclusions

The preceding sections emphasize the structural, mechanical, optical, and conductivity property differences observed in a dimorphic aromatic system having distinct molecular arrangements. The metastable block-shaped BZB form is an example of a disappearing polymorph; as with the appearance of BZN, we could not generate the former crystal form even after repeated attempts and varying conditions. The BZB with a stacked columnar arrangement and interrupted intercolumnar region hampered a continuous molecular movement. Not surprising that the nanoindentation experiments indicate a discontinuous plastic deformation mechanism in contrast to a continuous smooth *P*–*h* curve in the BZN crystals. The zig-zag layer arrangement in BZN and the accordion-type layer movement enabled a continuous layer deformation under the indenter tip. BZN with a higher magnitude of *H* and *E* than the metastable BZB further hints at the mechanical response as a possible determinant factor that affects the overall stability of the crystal form. Even though both the crystal forms exhibit blue emission, they differ in the luminescence quantum yields, lifetimes and band profile of the characteristic emissions. Because of the index contrast, the acicular crystals of BZN exhibited passive wave guiding properties; the collected images with and without filters confirmed the propagation of elastically scattered photons (green) and subsequent generation of inelastically scattered (orange) photons by the crystals. Upon measuring the electrical conductivity of the dimorphs, BZB crystals with extended π-stacking proved to be a semiconductor with good hole mobility, while the BZN with zig-zag crystal packing with limited stacking exhibited insulator characteristics. Also, the property is highly anisotropic that the ethyl-carboxylate chains effectively interrupt the electronic communication between nearby columnar π-stacks. DFT calculations on the single molecule and both crystal dimorphs were used to rationalize the experimentally observed photophysical and conductive data. Notably, molecular crystal polymorphs that are light-emitting with varying electric conductivity are less reported, and the majority of them are insulators. By elucidating the relationship between molecular structure

and resulting properties, our research contributes to the design and development of novel materials with tailored functionalities

Experimental Section:

Materials and Synthesis: All other reagents are of analytical grade and used as received from Aldrich, Alfa Aesar, and Samchun chemicals unless otherwise specified. The detailed synthetic methodology and spectral details are provided in the supporting information.

Characterization: Single crystal diffraction data were taken using a Rigaku Saturn 724+ HG diffractometer with monochromated Mo K_α radiation and processed using the Rigaku Crystal Clear software. The structure was solved using direct techniques, and the refinements were done using full-matrix least-squares on F^2 using the SHELXTL suite of programs and OLEX2.[55] The PLATON program[56] verifies that each of the dimorphs is distinct; the packing and conformational preferences of the molecules in the two structures differ.

Thermal analysis: A differential scanning calorimeter (TA Q2000) was used to examine sample crystallization and melting behavior. Each sample was carefully weighed in aluminum pans and exposed to a thermal scan from room temperature to 150°C at a rate of 5°C/min.

Nanoindentation: For the indentation experiments, a Hysitron nanoindenter (TI Premier, Minneapolis, USA) with an in-situ Scanning Probe Microscope (SPM) was employed. We measured the load, *P*, and displacement, *h*, while constantly monitoring and recording, with resolutions of 1 nN and 0.2 nm for the force and displacement, respectively. For the experiment, a Berkovich diamond indenter with a tip radius of 75 nm was employed. Before being indented, the flat sections of the crystal surfaces were scanned with the same indenter tip. At the highest load, a loading rate of 0.2 mN/s and a hold duration of 10 s were set. The indentation imprints were captured immediately after unloading to eliminate time-dependent elastic recovery of the remaining impression. The Oliver-Pharr method was used to analyze the *P*-*h* curves to obtain the elastic modulus, *E*, of the crystal in that orientation.[57] Hardness, *H*, was calculated by dividing the maximum indentation load, P_{max}, by the contact area, *A*.

Photophysical studies: The electronic absorption spectra of all samples were measured using a Mecasys Optizen Pop UV/vis spectrophotometer. Photoluminescence (PL) spectra were recorded by a JASCO spectrofluorimeter (FP-6500); emission and excitation spectra were corrected according to standard correction curves. Fluorescence lifetimes were measured using time-correlated single photon counting (TCSPC) equipment by Hamamatsu (C11367-31). The

photoluminescence quantum yield (Φ_f) of BZQ in solution was calculated using relative methods with quinine sulfate as a reference (Φ_f = 0.54);[58] while the solid-state quantum yields of BZN and BZB polymorphs were estimated using the Hamamatsu Quantaurus-QY absolute quantum yield spectrometer (C11347-11).

Computational studies: Density functional theory (DFT) calculations on the BZQ single molecule were carried out using the B.01 revision of the Gaussian 16 program package[59] in combination with the PBE0 generalized-gradient hybrid exchange-correlation functional, [60] and the def2-TZVP basis set of Ahlrichs and coworkers.[61] BZQ was fully optimized in the ground state (S_0) and in the lowest singlet state (S_1); frequency calculations were always used to confirm that every stationary point found by geometry optimizations was actually a minimum on the corresponding potential-energy surface (no imaginary frequencies). Time-dependent DFT calculations (TD-DFT)[62-64] were used to calculate the lowest 16 singlet excitations and their nature was assessed by the help of Natural Transition Orbital (NTO) analysis.[65] The same TD-DFT approach was also used for S_1 geometry optimization. All calculations were performed using the polarizable continuum model (PCM) to simulate dichloromethane solvation effects.[66-68] DFT calculations on the BZN and BZB crystals were carried out using Quantum ESPRESSO 7.0, the open-source suite for quantum simulation of materials.[69-71] The PBEsol GGA exchange–correlation functional[72] was chosen in combination with the semiempirical Grimme's DFT-D3 dispersion corrections with zero damping, [73] to take into account possible π–π interactions between nearby organic molecules. The pseudopotentials were directly taken from the SSSP Efficiency PBEsol pseudopotential library (version 1.1.2); [74,75] the kinetic energy cut-off of the wave function was set to 60 Ry and the one for charge density to 480 Ry, according to the adopted pseudopotential requirements. For all SCF calculations, the convergence threshold for self-consistency was set to $2.0 \cdot 10^{-10}$ Ry times the number of atoms in the cell. The initial guess for the structure of each compound was based on the experimental single-crystal X-ray diffraction data (directly taken from CIF files). All structures were fully relaxed using a variable-cell approach, using the BFGS (Broyden–Fletcher–Goldfarb–Shanno) algorithm. During the optimization, the only imposed constraint was to keep the crystal space group consistent with the experimental one, but both the cell parameters and ions were adjusted to obtain the minimum-energy structure; convergence threshold on total energy was set to $1.0 \cdot 10^{-5}$ Ry times the number of atoms in the cell, with forces acting on atoms below $1.0 \cdot 10^{-4}$ Ry/Bohr. For optimizations, the values for the K-point grid were selected so that the K-point distance in the reciprocal space was 0.3 $Å^{-1}$, as

implemented in the Materials Cloud platform.[76] The K-point grid sampling was increased to 0.2 $Å^{-1}$ for a higher-quality single-point SCF (self-consistent field) calculation on the optimized structure. For density-of-state (DOS) calculations, an even denser K-point grid was adopted in the corresponding NSCF (non-self-consistent field) calculation, imposing a K-point distance of 0.1 $Å^{-1}$. In order to obtain the band-structure diagrams, the first Brillouin zone was mapped along specific paths connecting both high-symmetry points and points related to important π–π planes in the direct lattice; K-points along the paths were sampled with a resolution of 0.03 $Å^{-1}$ using a home-made Python script.

The pictures showing single-molecule geometries and orbitals were created using GaussView 6.[77] For crystals, graphical visualization of selected wavefunction contributions to the pseudo-charge density at specific K-points was accomplished by VESTA (version 3.5.8).[78]

References

(1) Li, J.; Qin, Z.; Sun, Y.; Zhen, Y.; Liu, J.; Zou, Y.; Li, C.; Lu, X.; Jiang, L.; Zhang, X.; Ji, D.; Li, L.; Dong, H.; Hu, W. Regulating Crystal Packing by Terminal Tert-Butylation for Enhanced Solid-State Emission and Efficacious Charge Transport in an Anthracene-Based Molecular Crystal. *Angew. Chem. Int. Ed.* **2022,** *61,* e202206825.

(2) Wang, C.; Sun, C. C. The Landscape of Mechanical Properties of Molecular Crystals. *CrystEngComm* **2020,** *22,* 1149-1153.

(3) Mishra, M. K.; Ramamurty, U.; Desiraju, G. R. Mechanical Property Design of Molecular Solids. *Curr. Opin. Sol. St. Mater. Sci.* **2016,** *20,* 361-370.

(4) Commins, P.; Desta, I. T.; Karothu, D. P.; Panda, M. K.; Naumov, P. Crystals on the Move: Mechanical Effects in Dynamic Solids. *Chem. Commun.* **2016,** *52,* 13941-13954.

(5) Wang, K.; Zhang, H.; Chen, S.; Yang, G.; Zhang, J.; Tian, W.; Su, Z.; Wang, Y. Organic Polymorphs: One-Compound-Based Crystals With Molecular-Conformation- and Packing-Dependent Luminescent Properties. *Adv. Mater.* **2014,** *26,* 6168-6173.

(6) Hiew, S. H.; Lu, Y.; Han, H.; Gonçalves, R. A.; Alfarano, S. R.; Mezzenga, R.; Parikh, A. N.; Mu, Y.; Miserez, A. Modulation of Mechanical Properties of Short Bioinspired Peptide Materials by Single Amino-Acid Mutations. *J. Am. Chem. Soc.* **2023,** *145,* 3382-3393.

(7) Varghese, S.; Das, S. Role of Molecular Packing in Determining Solid-State Optical Properties of Π-Conjugated Materials. *J. Phys. Chem. Lett.* **2011,** *2,* 863-873.

(8) von Hippel, A. R. Molecular Designing of Materials. *Science* **1962,** *138,* 91-108.

(9) Varughese, S. Non-Covalent Routes to Tune the Optical Properties of Molecular Materials. *J. Mater. Chem. C* **2014,** *2*, 3499-3516.

(10) Yan, D.; Evans, D. G. Molecular Crystalline Materials With Tunable Luminescent Properties: From Polymorphs to Multi-Component Solids. *Mater. Horiz.* **2014,** *1*, 46-57.

(11) Shen, X. Y.; Wang, Y. J.; Zhao, E.; Yuan, W. Z.; Liu, Y.; Lu, P.; Qin, A.; Ma, Y.; Sun, J. Z.; Tang, B. Z. Effects of Substitution With Donor–Acceptor Groups on the Properties of Tetraphenylethene Trimer: Aggregation-Induced Emission, Solvatochromism, and Mechanochromism. *J. Phys. Chem. C* **2013,** *117*, 7334-7347.

(12) Cruz-Cabeza, A. J.; Bernstein, J. Conformational Polymorphism. *Chem. Rev.* **2014,** *114*, 2170-2191.

(13) Gentili, D.; Gazzano, M.; Melucci, M.; Jones, D.; Cavallini, M. Polymorphism As an Additional Functionality of Materials for Technological Applications at Surfaces and Interfaces. *Chem. Soc. Rev.* **2019,** *48*, 2502-2517.

(14) Price, S. L. From Crystal Structure Prediction to Polymorph Prediction: Interpreting the Crystal Energy Landscape. *Phys. Chem. Chem. Phys.* **2008,** *10*, 1996-2009.

(15) Bernstein, J. *Polymorphism in Molecular Crystals*; Oxford Univ. Press: New York, 2002.

(16) Chung, H.; Diao, Y. Polymorphism As an Emerging Design Strategy for High Performance Organic Electronics. *J. Mater. Chem. C* **2016,** *4*, 3915-3933.

(17) Ivnitski, D.; Amit, M.; Silberbush, O.; Atsmon-Raz, Y.; Nanda, J.; Cohen-Luria, R.; Miller, Y.; Ashkenasy, G.; Ashkenasy, N. The Strong Influence of Structure Polymorphism on the Conductivity of Peptide Fibrils. *Angew. Chem. Int. Ed.* **2016,** *55*, 9988-9992.

(18) *Polymorphism in the Pharmaceutical Industry*; Wiley-VCH: Weinheim, Germany, 2006.

(19) Raju, C.; Ramteke, G. R.; Jose, K. V. J.; Sureshan, K. M. Cascading Effect of Large Molecular Motion in Crystals: A Topotactic Polymorphic Transition Paves the Way to Topochemical Polymerization. *J. Am. Chem. Soc.* **2023,** *145*, 9607-9616.

(20) Bernstein, J. Polymorphism: A Perspective. *Cryst. Growth Des.* **2011,** *11*, 632-650.

(21) Braga, D.; Grepioni, F.; Maini, L. The Growing World of Crystal Forms. *Chem. Commun.* **2010,** *46*, 6232-6242.

(22) Liu, Z.; Zhang, G.; Zhang, D. Molecular Materials That Can Both Emit Light and Conduct Charges: Strategies and Perspectives. *Chem. Eur. J.* **2016,** *22*, 462-471.

(23) Sugawara, K.; Ono, T.; Yano, Y.; Suzuki, T.; Ishigaki, Y. Exceptionally Flexible Quinodimethanes With Multiple Conformations: Polymorph-Dependent Colour Tone and Emission of Crystals. *Mater. Chem. Front.* **2023,** *7*, 1591-1598.

(24) Mutai, T.; Shono, H.; Shigemitsu, Y.; Araki, K. Three-Color Polymorph-Dependent Luminescence: Crystallographic Analysis and Theoretical Study on Excited-State Intramolecular Proton Transfer (ESIPT) Luminescence of Cyano-Substituted Imidazo[1,2-a]Pyridine. *CrystEngComm* **2014,** *16,* 3890-3895.

(25) Roche, G. H.; Flot, D.; Moreau, J. J. E.; Dautel, O. J.; Filhol, J. S.; van der Lee, A. Packing Polymorphism Affecting the Optoelectronic Properties of a Π-Conjugated Organic Compound. *Cryst. Growth Des.* **2021,** *21,* 3850-3863.

(26) Bernstein, J.; Davey, R. J.; Henck, J. O. Concomitant Polymorphs. *Angew. Chem. Int. Ed.* **1999,** *38,* 3440-3461.

(27) Price, S. L. The Computational Prediction of Pharmaceutical Crystal Structures and Polymorphism. *Adv. Drug. Del. Rev.* **2004,** *56,* 301-319.

(28) Nangia, A. Conformational Polymorphism in Organic Crystals. *Acc. Chem. Res.* **2008,** *41*, 595-604.

(29) Vippagunta, S. R.; Brittain, H. G.; Grant, D. J. W. Crystalline Solids. *Adv. Drug. Del. Rev.* **2001,** *48,* 3-26.

(30) Grant, D. J. W. Theory and Origin of Polymorphism. In *Polymorphism in Pharmaceutical Solids*; Brittain, H. G., Ed.; Marcel Dekker, Inc.: New York, 1999; Vol. 95, Chapter 1.

(31) Dunitz, J. D.; Bernstein, J. Disappearing Polymorphs. *Acc. Chem. Res.* **1995,** *28,* 193-200.

(32) Bucar, D. K.; Lancaster, R. W.; Bernstein, J. Disappearing Polymorphs Revisited. *Angew. Chem. Int. Ed.* **2015,** *54,* 6972-6993.

(33) Bauer, J.; Spanton, S.; Henry, R.; Quick, J.; Dziki, W.; Porter, W.; Morris, J. Ritonavir: An Extraordinary Example of Conformational Polymorphism. *Pharm. Res.* **2001,** *18,* 859-866.

(34) Bernstein, J.; Henck, J. O. Disappearing and Reappearing Polymorphs: an Anathema to Crystal Engineering? *Crystal Engineering* **1998,** *1,* 119-128.

(35) Spackman, M. A.; Jayatilaka, D. Hirshfeld Surface Analysis. *CrystEngComm* **2008,** *11,* 19-32.

(36) Turner, M. J.; Thomas, S. P.; Shi, M. W.; Jayatilaka, D.; Spackman, M. A. Energy Frameworks: Insights into Interaction Anisotropy and the Mechanical Properties of Molecular Crystals. *Chem. Commun.* **2015,** *51,* 3735-3738.

(37) Burger, A.; Ramberger, R. On the Polymorphism of Pharmaceuticals and Other Molecular Crystals. I. *Microchim. Acta* **1979,** *72,* 259-271.

(38) Varughese, S.; Kiran, M. S. R. N.; Ramamurty, U.; Desiraju, G. R. Nanoindentation in Crystal Engineering: Quantifying Mechanical Properties of Molecular Crystals. *Angew. Chem. Int. Ed.* **2013,** *52,* 2701-2712.

(39) Varughese, S.; Kiran, M. S. R. N.; Solanko, K. A.; Bond, A. D.; Ramamurty, U.; Desiraju, G. R. Interaction Anisotropy and Shear Instability of Aspirin Polymorphs Established by Nanoindentation. *Chem. Sci.* **2011,** *2,* 2236-2242.

(40) Varughese, S.; Kiran, M. S. R. N.; Ramamurty, U.; Desiraju, G. R. Nanoindentation As a Probe for Mechanically-Induced Molecular Migration in Layered Organic Donor-Acceptor Complexes. *Chem. Asian J.* **2012,** *7,* 2118-2125.

(41) SeethaLekshmi, S.; Kiran, M. S. R. N.; Ramamurty, U.; Varughese, S. Molecular Basis for the Mechanical Response of Sulfa Drug Crystals. *Chem. Eur. J.* **2019,** *25,* 526-537.

(42) Borlido, P.; Schmidt, J.; Huran, A. W.; Tran, F.; Marques, M. l. A. L.; Botti, S. Exchange-Correlation Functionals for Band Gaps of Solids: Benchmark, Reparametrization and Machine Learning. *Npj Comput. Mater.* **2020,** *6,* 96.

(43) Hoffmann, R. How Chemistry and Physics Meet in the Solid State. *Angew. Chem. Int. Ed. Engl.* **1987,** *26,* 846-878.

(44) Yan, X.; Su, Y.; Li, J.; Früh, J.; Möhwald, H. Uniaxially Oriented Peptide Crystals for Active Optical Waveguiding. *Angew. Chem. Int. Ed.* **2011,** *50,* 11186-11191.

(45) Annadhasan, M.; Basak, S.; Chandrasekhar, N.; Chandrasekar, R. Next-Generation Organic Photonics: The Emergence of Flexible Crystal Optical Waveguides. *Adv. Optical Mater.* **2020,** *8,* 2000959.

(46) Chandrasekar, R. Organic Photonics: Prospective Nano/Micro Scale Passive Organic Optical Waveguides Obtained From Π-Conjugated Ligand Molecules. *Phys. Chem. Chem. Phys.* **2014,** *16,* 7173-7183.

(47) Chandrasekhar, N.; Mohiddon, M. A.; Chandrasekar, R. Organic Submicro Tubular Optical Waveguides: Self-Assembly, Diverse Geometries, Efficiency, and Remote Sensing Properties. *Adv. Optical Mater.* **2013,** *1,* 305-311.

(48) Basak, S.; Chandrasekar, R. Passive Optical Waveguiding Organic Rectangular Tubes: Tube Cutting, Controlling Light Propagation Distance and Multiple Optical Out-Puts. *J. Mater. Chem. C* **2014,** *2,* 1404-1408.

(49) Chandrasekhar, N.; Reddy, E. R.; Prasad, M. D.; Rajadurai, M. S.; Chandrasekar, R. Passive Optical Waveguiding Tubular Pharmaceutical Solids and Raman Spectroscopy/Mapping of Nano-/Micro-Scale Defects. *CrystEngComm* **2014,** *16,* 4696-4700.

(50) Dadvand, A.; Moiseev, A. G.; Sawabe, K.; Sun, W. H.; Djukic, B.; Chung, I.; Takenobu, T.; Rosei, F.; Perepichka, D. F. Maximizing Field-Effect Mobility and Solid-State Luminescence in Organic Semiconductors. *Angew. Chem. Int. Ed.* **2012,** *51,* 3837-3841.

(51) Ju, H.; Wang, K.; Zhang, J.; Geng, H.; Liu, Z.; Zhang, G.; Zhao, Y.; Zhang, D. 1,6- and 2,7-Trans-β-Styryl Substituted Pyrenes Exhibiting Both Emissive and Semiconducting Properties in the Solid State. *Chem. Mater.* **2017,** *29,* 3580-3588.

(52) Ray, K. K.; Campillo-Alvarado, G.; Morales-Rojas, H.; Höpfl, H.; MacGillivray, L. R.; Tivanski, A. V. Semiconductor Cocrystals Based on Boron: Generated Electrical Response With Π-Rich Aromatic Molecules. *Cryst. Growth Des.* **2020,** *20,* 3-8.

(53) Lim, J. M.; Kim, P.; Yoon, M. C.; Sung, J.; Dehm, V.; Chen, Z.; Würthner, F.; Kim, D. Exciton Delocalization and Dynamics in Helical Π-Stacks of Self-Assembled Perylene Bisimides. *Chem. Sci.* **2013,** *4,* 388-397.

(54) Kim, J. H.; Schembri, T.; Bialas, D.; Stolte, M.; Würthner, F. Slip-Stacked J-Aggregate Materials for Organic Solar Cells and Photodetectors. *Adv. Mater.* **2022,** *34,* 2104678.

(55) Sheldrick, G. M. A Short History of SHELX. *Acta Crystallogr. , Sect. A* **2008,** *64,* 112-122.

(56) Speck, A. L. PLATON. Acta Crystallogr., Sect.A A46, C34. 1990. Ref Type: Computer Program

(57) Oliver, W. C.; Pharr, G. M. An Improved Technique for Determining Hardness and Elastic Modulus Using Load and Displacement Sensing Indentation Experiments. *J. Mater. Res.* **1992,** *7,* 1564-1583.

(58) Brouwer, A. M. Standards for Photoluminescence Quantum Yield Measurements in Solution (IUPAC Technical Report). *Pure Appl. Chem.* **2011,** *83,* 2213-2228.

(59) Frisch, M. J.; Trucks, G. W.; Schlegel, H. B.; Scuseria, G. E.; Robb, M. A.; Cheeseman, J. R.; Scalmani, G.; Barone, V.; Petersson, G. A.; Nakatsuji, H.; Li, X.; Caricato, M.; Marenich, A. V.; Bloino, J.; Janesko, B. G.; Gomperts, R.; Mennucci, B.; Hratchian, H. P.; Ortiz, J. V.; Izmaylov, A. F.; Sonnenberg, J. L.; Williams, A.; Ding, F.; Lipparini, F.; Egidi, F.; Goings, J.; Peng, B.; Petrone, A.; Henderson, T.; Ranasinghe, D.; Zakrzewski, V. G.; Gao, J.; Rega, N.; Zheng, G.; Liang, W.; Hada, M.; Ehara, M.; Toyota, K.; Fukuda, R.; Hasegawa, J.; Ishida, M.; Nakajima, T.; Honda, Y.; Kitao, O.; Nakai, H.; Vreven, T.; Throssell, K.; Montgomery Jr, J. A.; Peralta, J. E.; Ogliaro, F.; Bearpark, M. J.; Heyd, J. J.; Brothers, E. N.; Kudin, K. N.; Staroverov, V. N.; Keith, T. A.; Kobayashi, R.; Normand, J.; Raghavachari, K.; Rendell, A. P.; Burant, J. C.; Iyengar, S. S.; Tomasi, J.; Cossi, M.; Millam, J. M.; Klene, M.; Adamo, C.; Cammi, R.; Ochterski, J. W.; Martin, R. L.; Morokuma, K.; Farkas, O.; Foresman, J. B.; Fox, D. J. Gaussian 16. [Rev. B.01]. 2016. Wallingford, CT, USA, Gaussian Inc.

(60) Adamo, C.; Barone, V. Toward Reliable Density Functional Methods Without Adjustable Parameters: The PBE0 Model. *J. Chem. Phys.* **1999,** *110,* 6158-6170.

(61) Weigend, F.; Ahlrichs, R. Balanced Basis Sets of Split Valence, Triple Zeta Valence and Quadruple Zeta Valence Quality for H to Rn: Design and Assessment of Accuracy. *Phys. Chem. Chem. Phys.* **2005,** *7,* 3297-3305.

(62) Stratmann, R. E.; Scuseria, G. E.; Frisch, M. J. An Efficient Implementation of Time-Dependent Density-Functional Theory for the Calculation of Excitation Energies of Large Molecules. *J. Chem. Phys.* **1998,** *109,* 8218-8224.

(63) Casida, M. E.; Jamorski, C.; Casida, K. C.; Salahub, D. R. Molecular Excitation Energies to High-Lying Bound States From Time-Dependent Density-

Functional Response Theory: Characterization and Correction of the Time-Dependent Local Density Approximation Ionization Threshold. *J. Chem. Phys.* **1998,** *108,* 4439-4449.

(64) Bauernschmitt, R.; Ahlrichs, R. Treatment of Electronic Excitations Within the Adiabatic Approximation of Time Dependent Density Functional Theory. *Chem. Phys. Lett.* **1996,** *256,* 454-464.

(65) Martin, R. L. Natural Transition Orbitals. *J. Chem. Phys.* **2003,** *118,* 4775-4777.

(66) Tomasi, J.; Persico, M. Molecular Interactions in Solution: An Overview of Methods Based on Continuous Distributions of the Solvent. *Chem. Rev.* **1994,** *94,* 2027-2094.

(67) Tomasi, J.; Mennucci, B.; Cammi, R. Quantum Mechanical Continuum Solvation Models. *Chem. Rev.* **2005,** *105,* 2999-3094.

(68) Cramer, C. J.; Truhlar, D. G. Continuum Solvation. Tapia, O., Bertrán, J., in Solent Effects and Chemical Reactivity, Eds.; Springer: Netherlands, 2002; Vol. 17, Chapter 1, 1-80.

(69) Giannozzi, P.; Baroni, S.; Bonini, N.; Calandra, M.; Car, R.; Cavazzoni, C.; Ceresoli, D.; Chiarotti, G. L.; Cococcioni, M.; Dabo, I.; Dal Corso, A.; de Gironcoli, S.; Fabris, S.; Fratesi, G.; Gebauer, R.; Gerstmann, U.; Gougoussis, C.; Kokalj, A.; Lazzeri, M.; Martin-Samos, L.; Marzari, N.; Mauri, F.; Mazzarello, R.; Paolini, S.; Pasquarello, A.; Paulatto, L.; Sbraccia, C.; Scandolo, S.; Sclauzero, G.; Seitsonen, A. P.; Smogunov, A.; Umari, P.; Wentzcovitch, R. M. QUANTUM ESPRESSO: a Modular and Open-Source Software Project for Quantum Simulations of Materials. *J. Phys. Condens. Matter* **2009,** *21,* 395502.

(70) Giannozzi, P.; Andreussi, O.; Brumme, T.; Bunau, O.; Buongiorno Nardelli, M.; Calandra, M.; Car, R.; Cavazzoni, C.; Ceresoli, D.; Cococcioni, M.; Colonna, N.; Carnimeo, I.; Dal Corso, A.; de Gironcoli, S.; Delugas, P.; DiStasio, R. A.; Ferretti, A.; Floris, A.; Fratesi, G.; Fugallo, G.; Gebauer, R.; Gerstmann, U.; Giustino, F.; Gorni, T.; Jia, J.; Kawamura, M.; Ko, H. Y.; Kokalj, A.; Kücükbenli, E.; Lazzeri, M.; Marsili, M.; Marzari, N.; Mauri, F.; Nguyen, N. L.; Nguyen, H. V.; Otero-de-la-Roza, A.; Paulatto, L.; Poncé, S.; Rocca, D.; Sabatini, R.; Santra, B.; Schlipf, M.; Seitsonen, A. P.; Smogunov, A.; Timrov, I.; Thonhauser, T.; Umari, P.; Vast, N.; Wu, X.; Baroni, S. Advanced Capabilities for Materials Modelling With Quantum ESPRESSO. *J. Phys. Condens. Matter* **2017,** *29,* 465901.

(71) Giannozzi, P.; Baseggio, O.; Bonfà, P.; Brunato, D.; Car, R.; Carnimeo, I.; Cavazzoni, C.; de Gironcoli, S.; Delugas, P.; Ferrari Ruffino, F.; Ferretti, A.; Marzari, N.; Timrov, I.; Urru, A.; Baroni, S. Quantum ESPRESSO Toward the Exascale. *J. Chem. Phys.* **2020,** *152,* 154105.

(72) John, P. P.; Adrienn, R.; Gábor, I. C.; Oleg, A. V.; Gustavo, E. S.; Lucian, A. C.; Xiaolan, Z.; Kieron, B. Restoring the Density-Gradient Expansion for Exchange in Solids and Surfaces. *Phys. Rev. Lett.* **2008,** *100,* 136406-1-136406-4.

(73) Grimme, S.; Antony, J.; Ehrlich, S.; Krieg, H. A Consistent and Accurate Ab Initio Parametrization of Density Functional Dispersion Correction (DFT-D) for the 94 Elements H-Pu. *J. Chem. Phys.* **2010,** *132,* 154104.

(74) Prandini, G.; Marrazzo, A.; Castelli, I. E.; Mounet, N.; Marzari, N. Precision and Efficiency in Solid-State Pseudopotential Calculations. *Npj Comput. Mater.* **2018,** *4,* 72.

(75) Lejaeghere, K.; Bihlmayer, G.; Björkman, T.; Blaha, P.; Blügel, S.; Blum, V.; Caliste, D.; Castelli, I. E.; Clark, S. J.; Dal Corso, A.; de Gironcoli, S.; Deutsch, T.; Dewhurst, J. K.; Di Marco, I.; Draxl, C.; Dulak, M.; Eriksson, O.; Flores-Livas, J. A.; Garrity, K. F.; Genovese, L.; Giannozzi, P.; Giantomassi, M.; Goedecker, S.; Gonze, X.; Gränäs, O.; Gross, E. K. U.; Gulans, A.; Gygi, F.; Hamann, D. R.; Hasnip, P. J.; Holzwarth, N. A. W.; Iusan, D.; Jochym, D. B.; Jollet, F.; Jones, D.; Kresse, G.; Koepernik, K.; Kücükbenli, E.; Kvashnin, Y. O.; Locht, I. L. M.; Lubeck, S.; Marsman, M.; Marzari, N.; Nitzsche, U.; Nordström, L.; Ozaki, T.; Paulatto, L.; Pickard, C. J.; Poelmans, W.; Probert, M. I. J.; Refson, K.; Richter, M.; Rignanese, G. M.; Saha, S.; Scheffler, M.; Schlipf, M.; Schwarz, K.; Sharma, S.; Tavazza, F.; Thunström, P.; Tkatchenko, A.; Torrent, M.; Vanderbilt, D.; van Setten, M. J.; Van Speybroeck, V.; Wills, J. M.; Yates, J. R.; Zhang, G. X.; Cottenier, S. Reproducibility in Density Functional Theory Calculations of Solids. *Science* **2016,** *351,* aad3000-1-aad3000-7.

(76) Talirz, L.; Kumbhar, S.; Passaro, E.; Yakutovich, A. V.; Granata, V.; Gargiulo, F.; Borelli, M.; Uhrin, M.; Huber, S. P.; Zoupanos, S.; Adorf, C. S.; Andersen, C. r. W.; Schütt, O.; Pignedoli, C. A.; Passerone, D.; VandeVondele, J.; Schulthess, T. C.; Smit, B.; Pizzi, G.; Marzari, N. Materials Cloud, a Platform for Open Computational Science. *Sci. Data* **2020,** *7,* 299.

(77) Dennington, R.; Keith, T. A.; Millam, J. M. Gaussview, Version 6, 2016. Shawnee Mission, KS, USA., Semichem Inc.

(78) Momma, K.; Izumi, F. VESTA 3 for Three-Dimensional Visualization of Crystal, Volumetric and Morphology Data. *J. Appl. Cryst.* **2011,** *44,* 1272-1276.

Table of Contents

Dimorphs of a Benzothiophene-quinoline Derivative with Distinct Mechanical, Optical, Photophysical and Conducting Properties

K. S. Bejoymohandas, Ashish, Chithra H. Sharma, Seetha Lekshmi Sunil, M. S. R. N. Kiran, Indira S. Divya, Madhu Thalakulam*, Filippo Monti*, Rajesh V. Nair*, Sunil Varughese*

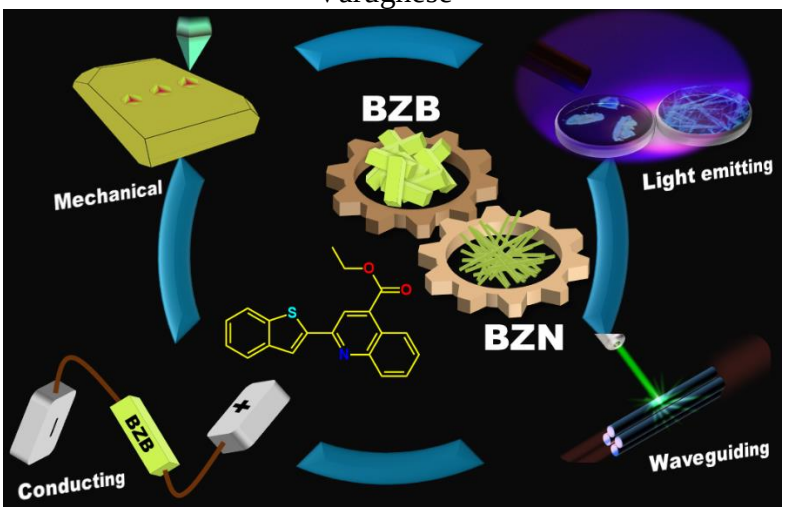

Dimorphs of ethyl-2-(1-benzothiophene-2-yl)quinolone-4-carboxylate exhibit distinct molecular arrangments and hence vary in their mechanical, conducting, photophysical and waveguiding properties, highlighting the significant role of polymorphism in modulating the functional properties in molecular materials.